

# The origin of S0s in clusters: evidence from the bulge and disc star formation histories

Evelyn J. Johnston,<sup>1\*</sup> Alfonso Aragón-Salamanca<sup>1</sup> and Michael R. Merrifield<sup>1</sup>

<sup>1</sup>*School of Physics and Astronomy, University of Nottingham, University Park, Nottingham, NG7 2RD, UK*

6 May 2019

## ABSTRACT

The individual star formation histories of bulges and discs of lenticular (S0) galaxies can provide information on the processes involved in the quenching of their star formation and subsequent transformation from spirals. In order to study this transformation in dense environments, we have decomposed long-slit spectroscopic observations of a sample of 21 S0s from the Virgo Cluster to produce one-dimensional spectra representing purely the bulge and disc light for each galaxy. Analysis of the Lick indices within these spectra reveals that the bulges contain consistently younger and more metal-rich stellar populations than their surrounding discs, implying that the final episode of star formation within S0s occurs in their central regions. Analysis of the  $\alpha$ -element abundances in these components further presents a picture in which the final episode of star formation in the bulge is fueled using gas that has previously been chemically enriched in the disc, indicating the sequence of events in the transformation of these galaxies. Systems in which star formation in the disk was spread over a longer period contain bulges in which the final episode of star formation occurred more recently, as one might expect for an approximately coeval population in which the transformation from spiral to S0 occurred at different times. With data of this quality and the new analysis method deployed here, we can begin to describe this process in a quantitative manner for the first time.

**Key words:** galaxies: elliptical and lenticular – galaxies: evolution – galaxies: formation – galaxies: stellar content

## 1 INTRODUCTION

Lenticular galaxies (S0s) lie between spirals and ellipticals on the Hubble Sequence, sharing the discy morphology of the spiral galaxies but containing the redder colours and old stellar populations generally seen in ellipticals. As a result, they are often seen as a transitional phase between spirals and ellipticals, and so understanding their formation is key to understanding the evolution of galaxies and the significance of the Hubble Sequence.

Plenty of evidence exists to suggest an evolutionary link between spirals and S0s. The morphology–density relation of Dressler (1980) showed that spirals tend to dominate lower density regions of space, such as the field, while S0s begin to dominate as you move into groups and clusters. This finding suggests that the local environment plays a key role in the transformation of spirals to S0s, where the higher frequency of interactions in groups and clusters contribute significantly to the quenching of star formation in the progenitor spirals. Studies such as Dressler et al. (1997), Fasano et al. (2000) and Desai et al. (2007) have also found a link with redshift, where the fraction of S0s increased toward lower red-

shifts while that of spirals decreased, thus revealing that S0s are more common at more recent epochs than in the past.

Many processes have been suggested to explain this transformation, most of which focus on an interaction that quenches the star formation in the disc followed by passive evolution as the galaxy fades to an S0. The interaction that triggers the transformation could be with the intra-cluster medium as the galaxy travels through the cluster, where the disc gas is removed by ram pressure stripping (Gunn & Gott 1972) or the halo gas is stripped and the star formation quenched by starvation (Larson, Tinsley & Caldwell 1980; Bekki, Shioya & Couch 2002). Alternatively, interactions with neighbouring galaxies could lead to the gas being stripped by harassment (Moore et al. 1996; Moore, Lake & Katz 1998; Moore et al. 1999), or minor mergers could initiate starbursts that use up all of the remaining gas throughout the entire disc (Mihos & Hernquist 1994). It is still uncertain whether any one of these processes dominate the transformation, or if the process changes with time, environment or luminosity. Evidence that such variations do occur was found by Barway et al. (2007, 2009), who found that the transformation process is dependent on the luminosity of the galaxy, where fainter S0s evolved through secular processes while brighter galaxies were created by more turbulent ones.

\* Email: Evelyn.Johnston@nottingham.ac.uk

The different processes that have been suggested to explain the transformation of spirals to S0s would affect the bulges and discs in different ways, making their individual star formation histories key to understanding the transformation process. For this reason, many studies have tried looking at variations in the stellar populations of S0s between the bulge and disc for clues to the transformation process that created that galaxy. One way of looking at the stellar populations is to use multi-waveband photometry to measure colour gradients over the galaxy, which provides information on the stellar populations as younger and lower-metallicity stars tend to emit bluer light. Terndrup et al. (1994), Peletier & Balcells (1996) and Möllenhoff (2004) all found evidence of negative colour gradients within the bulges of S0s and spirals, suggesting that redder light, and therefore older or more metal-rich stellar populations, are more centrally concentrated within these galaxies. Similarly, Bothun & Gregg (1990), Peletier & Balcells (1996) and Hudson et al. (2010) found that the discs of S0s and spirals are bluer than the bulges, suggesting that disc galaxies either experienced more recent star formation at larger radii (de Jong 1996), or have higher metallicities in their nuclear regions (Beckman et al. 1996; Pompei & Natali 1997).

Spectroscopic studies of galaxies have also been used to study stellar population gradients across the bulges and discs of S0s. For example, negative metallicity gradients and positive age gradients have been detected in S0s by Fisher, Franx & Illingworth (1996), Bell & de Jong (2000), Prochaska Chamberlain et al. (2011) and Bedregal et al. (2011), which indicate that the central regions of S0s contain younger and more metal rich stars. Further evidence of recent star formation in bulge regions of S0s has been detected by Poggianti et al. (2001), Ferrarese et al. (2006), Sil'Chenko (2006) and Kuntschner et al. (2006), and a study by Pracy et al. (2013) found evidence of strong positive age gradients within the central  $\sim 1$  kpc of the bulges of 'k+a' galaxies, which are thought to be a transitional phase between spirals and S0s. Another recent study of 'k+a' galaxies by Rodríguez Del Pino et al. (2014) also found evidence that the most recent star formation activity in these galaxies was centrally concentrated within the disc, and that the transformation from spirals most likely arose through gentler processes such as ram-pressure stripping or galaxy-galaxy interactions.

Such studies of the star formation histories of S0 bulges and discs have revealed age and metallicity gradients across the galaxies, but fail to provide information on whether it represents a gradient within the individual components, or whether it arises simply from the superposition of varying amounts of bulge and disc light, where each component contains stellar populations of distinct different ages and metallicities. To overcome these limitations, we have developed a new method for spectroscopic bulge–disc decomposition (Johnston et al. 2012), in which a high-quality spectrum of a galaxy is cleanly separated into bulge and disc components wavelength-by-wavelength to create two, one-dimensional spectra representing purely the bulge and disc light. These clean spectra can then be analyzed to determine the ages and metallicities of the bulge and disc with minimal contamination in order to determine the sequence of star-formation events that led to the formation of the S0.

In this paper, we set out to analyze the bulge and disc star formation histories spectroscopically for a sample of S0s from the Virgo Cluster, in order to determine the process that triggered their transformation from spirals. The Virgo Cluster was selected as the closest single system with sufficient members to undertake a systematic study of this transformation process. Section 2 describes the data set and reduction, and Section 3 summarizes the method.

The results for the stellar populations analysis, the star formation timescales and chemical enrichment are discussed in Section 4. The implications of these results for the likely evolutionary tracks followed by S0s are discussed in Section 5.

## 2 OBSERVATIONS AND DATA REDUCTION

In order to study the transformation of spirals to S0s in clusters, we adopted a sample of 21 luminosity-selected S0s from the ACS Virgo Cluster Survey (Côté et al. 2004). Details of the full sample are given in Table 1. The data set covers absolute B-band magnitudes in the range of  $-22.3 < M_B < -17.3$ , with galaxy inclinations of greater than  $40^\circ$ , where  $90^\circ$  is edge on, in order to minimize contamination from elliptical galaxies.

The galaxies were observed along their major axis using the GMOS instruments (Hook et al. 2004) in long-slit mode on Gemini-North and Gemini-South between 2008 April 24 and 2011 June 20. In a number of cases, the centres of the larger galaxies were offset from the middle of the slit in order to maximize the spatial coverage. The B1200 grating was used in combination with a 0.5 arcsec slit. A central wavelength of  $\sim 4730$  Å, slightly offset between the two sets of exposures to fill in the gaps between the chips, gave a wavelength range of  $\sim 4300 - 5450$  Å with a dispersion of  $0.235$  Å pixel $^{-1}$ . The spectral resolution was measured from the FWHM of the arc lines to be  $\sim 1.13$  Å, which corresponds to a velocity resolution of  $72$  km s $^{-1}$  FWHM. Spatially, the CCDs were binned by 4 to give a final scale of  $0.29$  arcseconds pixel $^{-1}$ .

A series of spectrophotometric and template stars were also observed with the same instrumental set up, of which the details are given in Table 2. The template stars were selected to cover a range of spectral types in order to match the composite spectral type of the galaxy during the kinematic analysis.

Calibration flat fields and CuAr arc spectra were taken following each set of observations with the same instrumental set-up, and the spectra were reduced using the GMOS spectral reduction packages in IRAF.<sup>1</sup> All the science and calibration frames were reduced by applying bias subtraction, flat field correction, cosmic ray removal and an initial wavelength calibration, and the three sections of each spectrum from each CCD were joined together. The arc spectra were then used to correct for the geometric distortions caused by the instrument optics and to refine the wavelength solution over the whole spectrum; the residuals of the resulting wavelength fits were generally  $\sim 0.2 - 0.3$  Å.

The wavelength-calibrated spectra were then sky subtracted and corrected for atmospheric extinction before flux calibration using the spectrophotometric standard star spectra. One standard star was observed for each programme of observations, and so all the galaxies observed as part of that programme were flux calibrated with the same stellar spectrum. Finally, the spectra from each galaxy were combined, using the measured positions of prominent sky lines to ensure the best possible registration of absolute wavelength calibration.

<sup>1</sup> IRAF is distributed by the National Optical Astronomy Observatories, which are operated by the Association of Universities for Research in Astronomy, Inc., under cooperative agreement with the National Science Foundation

**Table 1.** Sample of S0s from the Virgo Cluster.

Name	RA ( <sup>h</sup> <sup>m</sup> <sup>s</sup> )	dec ( <sup>°</sup> <sup>'</sup> <sup>''</sup> )	B <sub>T</sub>	Exp. Time (s)	Date	Telescope
(1)	(2)	(3)	(4)	(5)	(6)	(7)
VCC 798	12 25 24.04	+18 11 25.90	10.09	4 × 900	2009 February 26	Gemini-North
VCC 1535	12 34 03.10	+07 41 59.00	10.61	2 × 900	2009 February 26	Gemini-North
				2 × 900	2009 February 28	Gemini-North
VCC 2095	12 52 56.00	+11 13 53.00	11.18	4 × 900	2010 June 01	Gemini-North
VCC 1062	12 28 03.90	+09 48 14.00	11.40	4 × 900	2010 January 18	Gemini-South
VCC 2092	12 52 17.50	+11 18 50.00	11.51	1 × 900	2009 February 21	Gemini-North
				3 × 900	2009 February 26	Gemini-North
VCC 759	12 24 55.50	+11 42 15.00	11.80	5 × 900	2010 June 02	Gemini-North
				1 × 900	2010 July 08	Gemini-North
VCC 1692	12 36 53.40	+07 14 47.00	11.82	4 × 1000	2010 February 13	Gemini-South
VCC 2000	12 44 31.95	+11 11 25.10	11.94	4 × 900	2010 February 11	Gemini-South
VCC 685	12 23 57.90	+16 41 37.00	11.99	4 × 900	2010 March 11	Gemini-North
VCC 1664	12 36 26.86	+11 26 20.60	12.02	2 × 900	2009 April 27	Gemini-North
				2 × 900	2009 April 28	Gemini-North
VCC 944	12 26 50.53	+09 35 02.00	12.08	4 × 900	2009 April 23	Gemini-North
VCC 1938	12 42 47.40	+11 26 33.00	12.11	1 × 900	2009 April 29	Gemini-North
				3 × 900	2009 June 20	Gemini-North
VCC 1720	12 37 30.61	+09 33 18.80	12.29	3 × 1500	2011 May 30	Gemini-North
				2 × 1500	2011 June 04	Gemini-North
				1 × 1500	2011 June 20	Gemini-North
VCC 1619	12 35 30.61	+12 13 15.40	12.50	2 × 900	2009 June 20	Gemini-North
				2 × 900	2010 February 13	Gemini-South
VCC 1883	12 40 32.70	+07 18 53.00	12.57	2 × 1500	2011 May 25	Gemini-North
				1 × 1500	2011 May 27	Gemini-North
				3 × 1500	2011 May 28	Gemini-North
VCC 1242	12 29 53.49	+14 04 07.00	12.60	6 × 900	2010 February 23	Gemini-South
VCC 1250	12 29 59.10	+12 20 55.00	12.91	1 × 900	2009 April 19	Gemini-North
				3 × 900	2009 June 20	Gemini-North
VCC 1303	12 30 40.64	+09 00 55.90	13.10	3 × 1500	2010 July 13	Gemini-North
				1 × 1500	2010 July 15	Gemini-North
VCC 1913	12 42 10.70	+07 40 37.00	13.22	4 × 900	2010 February 22	Gemini-South
VCC 698	12 24 05.00	+11 13 06.00	13.60	4 × 1800	2009 February 28	Gemini-North
				1 × 1800	2009 April 23	Gemini-North
				5 × 1800	2009 April 28	Gemini-North
VCC 1833	12 40 19.65	+15 56 07.20	14.54	2 × 900	2010 February 13	Gemini-South

Note. Column (1): Galaxy name from Binggeli, Sandage & Tammann (1985); Column (2): RA; Column (3): Declination; Column (4): Total apparent blue-band magnitude from Binggeli, Sandage & Tammann (1985); Column (5): Exposure time in seconds; Column (6): Date of observations; Column (7): Telescope

**Table 2.** Spectrophotometric (S) and template (T) stars.

Name	T/S	Spectral Class
HD054719	T	K2 III
HD070272	T	K5 III
HD072324	T	G9 III
HD073593	T	G8 IV
HD120136	T	F6 IV
HD144872	T	K3 V
HD145148	T	K0 IV
HD161817	T	A2 VI
Feige66	S	-
Hiltner600	S	-
LTT1788	S	-

### 3 SPECTROSCOPIC BULGE–DISC DECOMPOSITION

#### 3.1 The method

In order to study the star formation histories of the bulge and disc, it was first necessary to separate the light into individual bulge and disc spectra by spectroscopic bulge–disc decomposition (Johnston et al. 2012). In brief, this method involves taking the light profile of the galaxy at each wavelength in the spectrum, and fitting a bulge and disc light profile to this distribution in the same manner as for one-dimensional photometric bulge–disc decomposition. The bulge was modeled as a Sérsic profile,

$$I(R) = I_e \exp \left\{ -b_n \left[ (R/R_e)^{1/n} - 1 \right] \right\}, \quad (1)$$

where  $R_e$  is the bulge effective radius,  $I_e$  is the bulge effective surface brightness,  $n$  is the sérsic index and  $b_n$  is a variable related to  $n$  (Sérsic 1968), while the disc was modeled as the exponential profile,

$$I(R) = I_0 \exp(-R/R_0), \quad (2)$$

**Table 3.** Results for the kinematics and decomposition parameters.

Name	$R_e$ [arcsec]	$R_0$ [arcsec]	$n$	$V_{LOS}$ [km s $^{-1}$ ]	$\sigma_0$ [km s $^{-1}$ ]
(1)	(2)	(3)	(4)	(5)	(6)
VCC 798	$8.9 \pm 0.3$	$61.5 \pm 0.6$	$1.87 \pm 0.14$	$688 \pm 5$	$181 \pm 7$
VCC 1062	$8.7 \pm 0.2$	$36.5 \pm 0.6$	$1.30 \pm 0.09$	$452 \pm 4$	$199 \pm 7$
VCC 2092	$8.74 \pm 0.15$	$67 \pm 2$	$1.41 \pm 0.07$	$1316 \pm 4$	$194 \pm 8$
VCC 1692	$4.5 \pm 0.4$	$22.4 \pm 0.3$	$1.6 \pm 0.4$	$1727 \pm 3$	$217 \pm 6$
VCC 2000	$2.43 \pm 0.05$	$9.7 \pm 0.7$	$0.91 \pm 0.08$	$1052 \pm 5$	$267 \pm 8$
VCC 685	$2.87 \pm 0.16$	$16.39 \pm 0.14$	$0.8 \pm 0.2$	$1159 \pm 5$	$200 \pm 8$
VCC 1664	$9 \pm 3$	$19.9 \pm 0.3$	$3.5 \pm 1.4$	$1118 \pm 10$	$207 \pm 17$
VCC 944	$14 \pm 5$	$31.4 \pm 0.5$	$3.9 \pm 1.1$	$834 \pm 4$	$146 \pm 5$
VCC 1720	$7.4 \pm 0.5$	$38.0 \pm 1.7$	$1.9 \pm 0.4$	$2316 \pm 2$	$119 \pm 3$
VCC 1883	$2.9 \pm 0.4$	$145 \pm 2$	$2.3 \pm 0.4$	$1767 \pm 1.3$	$77 \pm 2$
VCC 1242	$3.2 \pm 0.2$	$15.7 \pm 0.2$	$0.6 \pm 0.2$	$1530 \pm 2$	$80 \pm 3$
VCC 1303	$7 \pm 2$	$27 \pm 3$	$2.1 \pm 0.6$	$897 \pm 4$	$91 \pm 6$
VCC 698	$8 \pm 4$	$22.4 \pm 1.4$	$2.4 \pm 1.4$	$2079 \pm 2$	$52 \pm 2$

Note. Column (1): Galaxy name; Column (2): Bulge effective radius; Column (3): Disc scale length; (4): Bulge Sérsic index; Column (5): Central line-of-sight velocity; Column (6): Central velocity dispersion.

where  $I_0$  is the central surface brightness of the disc and  $R_0$  is the disc scale length (Freeman 1970). When decomposing spectra, the light profiles were fitted from a radius of 2 arcsec in order to minimize distortion of the light profile from the point-spread function in the central regions of the galaxy.

The bulge and disc parameters at each wavelength were integrated to obtain the total light from each component at that wavelength, and then plotted against wavelength to produce the one-dimensional bulge and disc spectra. Examples of the decomposed bulge and disc spectra for each galaxy in the sample are plotted in Fig. 1. To ensure that the light profile is derived from the same rest-frame wavelength at all radii, thus allowing a reliable decomposition at that wavelength, the spectrum was first corrected for radial velocity and velocity dispersion variations over the radius of the galaxy. The velocity dispersion was equalized by convolving the spectrum at each radius with the appropriate Gaussian to bring it up to the maximum value measured within the galaxy. The radial velocity correction was then applied by measuring the velocity offset from the centre of the galaxy by cross correlation, and applying a rolling average to the shifts to produce a smooth velocity curve from which the correction was measured. In the outer regions of the galaxy where noise dominates the spectrum, the last reliable shift in velocity was applied. If these kinematics corrections are applied correctly, then the final bulge and disc spectra would be expected to have matched line-of-sight velocities and velocity dispersions, which would correspond to the line-of-sight velocity at the centre of the galaxy and the maximum velocity dispersion measured within the galaxy. Therefore, the kinematics of these spectra were tested for each galaxy using the Penalized Pixel Fitting method (PPXF) of Cappellari & Emsellem (2004). PPXF uses the template stellar spectra from Table 2 to produce best fit models to the bulge and disc spectra by modeling the line-of-sight velocity distribution as a Gaussian with a series of Gauss-Hermite polynomials. The results for the bulge and disc were found to be consistent, and the values determined in this way are given in Table 3.

Many of galaxies within the sample were only slightly offset from the centre of the slit, allowing independent decomposition of both their semi-major axes. This repeated analysis was useful to check the reliability of the results by ensuring that they were consistent with each other. It was found that if all the bulge and disc pa-

rameters were left free for the fit, the results became very unstable, we believe due to a combination of degeneracy issues from leaving too many free parameters in the fits, and residual scattered light in the spectra. To reduce the degeneracy, the light profiles were fitted with fixed values for  $R_e$ ,  $R_0$  and  $n$ , where these quantities were measured from a fit to the mean light profile from the entire spectrum; the results for these decomposition parameters are given in Table 3. Examples of the light profile fits using these parameters are given in Fig. 2, which presents examples of the best fit to the mean light profile for VCC 698, and the fits achieved for individual light profiles from the continuum and within the H $\beta$  absorption feature. With this added constraint, the results from both semi-major axes became consistent with each other, and the co-added bulge and disc spectra bore a close resemblance to the original spectrum.

It was also hoped that by holding these parameters fixed in the fits, the effects of any residual scattered light could be mitigated. Since the physical distribution of the scattered light on the CCD is independent of the position of the galaxy on the CCD, we expected to obtain different results when decomposing both semi-major axes of each galaxy if significant amounts of scattered light was present. Therefore, the consistency in the results, both in terms of the decomposition parameters and the resultant stellar populations and alpha-enrichment analysis presented in Sections 4.1 and 4.2, suggests that the results presented here are not affected significantly by contamination from residual scattered light.

It was already found in Johnston et al. (2012) that this method for decomposition was limited to galaxies with high signal-to-noise ratios and with clean light profiles that could be approximated by the simple bulge + disc model. Of the 21 galaxies within the current data set, thirteen could be decomposed reliably using this method. Of the remaining eight, four (VCC 2095, VCC 759, VCC 1913 and VCC 1938) showed more complicated light profiles due to the presence of dust lanes, secondary discs, rings etc that could not be fitted by the simple bulge + disc model used here, and the faintest galaxy in the sample, VCC 1833, had too low a signal-to-noise ratio to fit both components reliably. In addition, VCC 1535 and VCC 1250 also show significant H $\beta$ , [OIII] $_{\lambda 4959}$  and [OIII] $_{\lambda 5007}$  emission originating from nuclear discs in their central regions, which could not be accounted for in the the light profiles with the simple model used in this study. The final recalcitrant galaxy

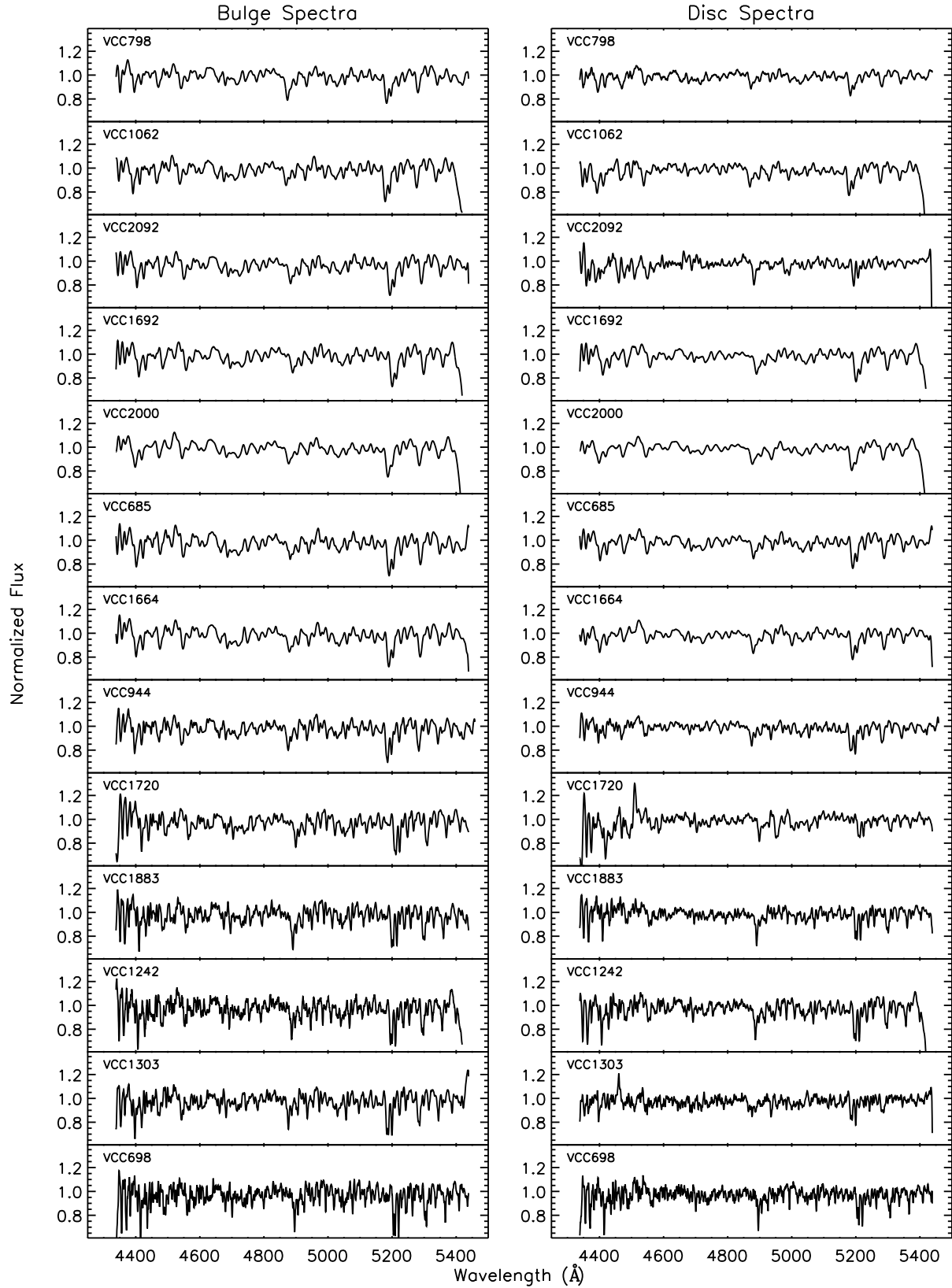
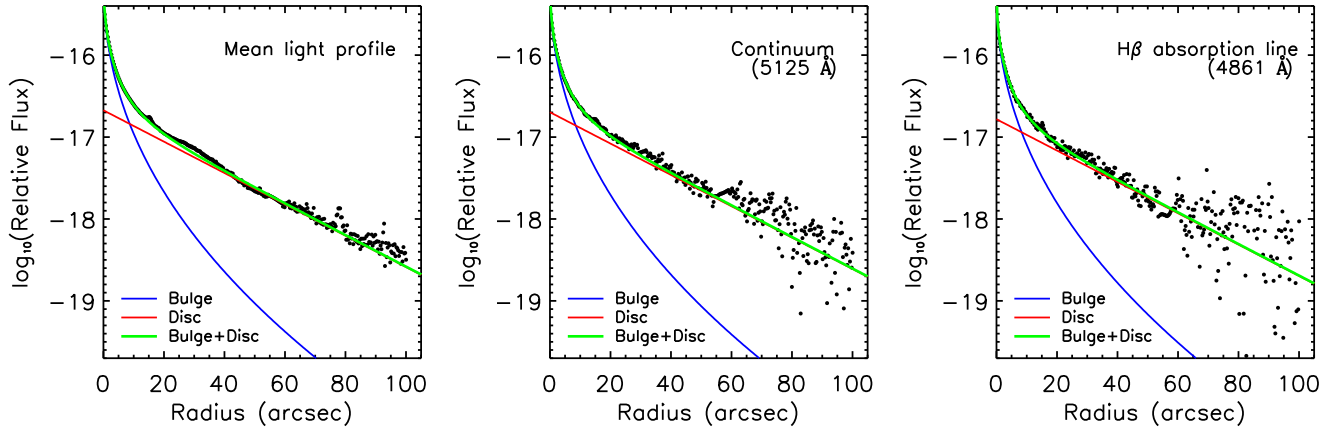


Figure 1. The decomposed bulge and disc spectra for the galaxies that could be decomposed with the Sersic bulge + exponential disc model.



**Figure 2.** The best fits to the mean light profile for VCC 698 (left), and example light profiles taken from the continuum (middle) and within the  $H\beta$  absorption feature (right). The bulge, disc and bulge + disc profiles are represented by the blue, red and green lines respectively.

was VCC 1619, which contains two counter-rotating stellar discs of similar mass and size, making it unsuitable for this type of decomposition. A separate decomposition of the stellar populations of the two discs in this bizarre galaxy was carried out using their kinematics, which is described in Johnston et al. (2013).

### 3.2 Comparison with decomposition of SDSS images

The method outlined in Section 3.1 is restricted by the use of long-slit spectra of the major axis only, which may introduce contamination in the stellar populations analysis due to the presence of structures such as dust lanes, bars, rings etc. that lie in the plane of the disc. More sophisticated methods of 2-D bulge–disc decomposition applied to images of galaxies have the advantage that they can work around such features and thus obtain better measurements of the bulge and disc parameters using the full structural information available. It would therefore be interesting to see whether our simpler 1-D decomposition could be compromising the extracted spectra.

To this end, full images of each galaxy were obtained from the SDSS DR7 (Abazajian et al. 2009), and mosaiced together with the MONTAGE software<sup>2</sup> to produce a large enough field of view for a 2-D photometric decomposition. The SDSS g-band images were selected because the central wavelength of this band, 4770 Å, lies closest to the central wavelength of the spectra, and the corrected (fpC) frames were used, and they had already undergone bias subtraction and flat fielding as part of the *frames* pipeline (Stoughton et al. 2002).

The decomposition was carried out using the GALFIT image analysis software (Peng et al. 2002, 2010, v3.0.4), which is a 2D parametric galaxy fitting algorithm. In order to compare directly to the spectral decompositions, the SDSS images were fitted with a Sérsic bulge and exponential disc profile. Each fit was also convolved with a PSF created for each galaxy by median stacking images of stars within the mosaiced image. The best fit model of each image and the residuals produced by GALFIT were checked by eye, and the software re-run with new initial parameters if the provisional fit was found to be poor. The results for the bulge and disc sizes and bulge Sérsic index were then compared with those from

the spectral decomposition, which produced a good correlation between the two methods with a low level of scatter which could be attributable to features within the plane of the disc as outlined above. As a further test of the impact of such systematic distortions, the spectra were decomposed again using fixed values for  $R_e$ ,  $R_0$  and  $n$  from the decomposition of the SDSS images and allowing only the amplitudes of the components to vary. This test revealed little difference between the bulge and disc ages and metallicities from the original spectroscopic decomposition results (see Sec. 4) and those decomposed using the SDSS values, thus confirming that the spectral decomposition is fairly robust against such modest systematic errors in the bulge and disc parameters.

### 3.3 Analysis of the systematic errors due to kinematics

Another potential issue with the decomposition method is that the kinematic corrections applied before the decomposition could result in losing information on the bulge and disc star formation histories. For example, by broadening the spectrum to match the maximum velocity dispersion, information on the line strengths in the outer regions may be lost, resulting in less reliable measurements of the line indices, and thus compromising the stellar populations analysis. Similarly, the radial velocity corrections were carried out by measuring the overall offset in the spectrum from the centre of the galaxy, which does not take into account the different rotational velocities that the bulge and disc will have.

In order to test the significance of these effects when decomposing the corrected two-dimensional spectrum, a series of simulated spectra were created and decomposed in the same way as the galaxy spectra. The model spectra were formed by co-adding spectra of known different stellar populations and velocity dispersions to represent the bulge and disc, where these spectra were obtained from the MILES stellar library (Sánchez-Blázquez et al. 2006). The proportion of bulge and disc light to add at each radius was determined by creating a model light profile based on typical measurements from the decomposition of the Virgo Cluster S0s, and the disc spectrum offset in the wavelength direction in order to simulate the rotational velocity of that component relative to a non-rotating model. As a final step, noise was added to the model spectra to simulate the uncertainties in the measurements.

The simulated spectra were then decomposed in the same way as the galaxy spectra, and the stellar populations of the bulges and

<sup>2</sup> <http://montage.ipac.caltech.edu/>

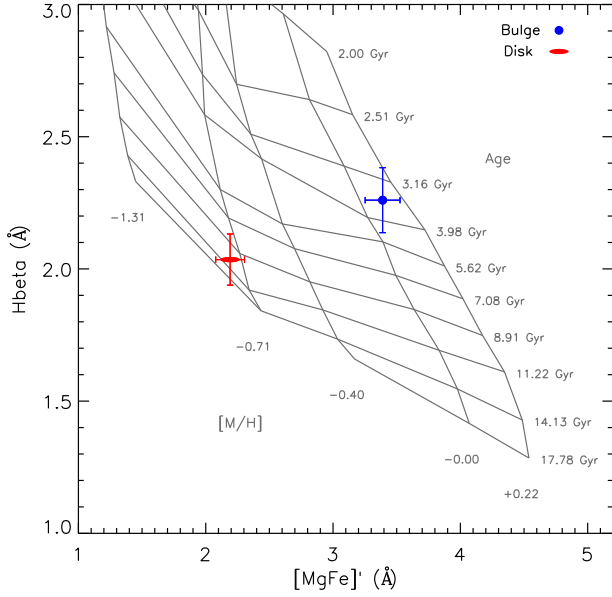


**Figure 3.** Example of the VCC 698 SSP model, with the line index measurements from the bulge and disc spectra over-plotted. The blue circle represents the bulge while the red ellipse corresponds to the disc value. The error bars represent the statistical uncertainties.

discs compared to the input values. The results were found to be consistent with the original stellar populations that went into the spectrum, thus indicating that the kinematic corrections described in Sec. 3.1 are sufficient to blur the individual kinematics of the bulge and disc to allow successful decomposition, while minimizing the information lost about the strengths of any features in the data.

## 4 STELLAR POPULATION ANALYSIS

### 4.1 Age and metallicity measurements

In order to extract the information on age and metallicity in the one-dimensional bulge and disc spectra, we used the hydrogen, magnesium and iron absorption line strengths as indicators of age and metallicity. The strengths of these absorption features were measured with the INDEXF software (Cardiel 2010), which uses the Lick/IDS index definitions to calculate a pseudo-continuum over each absorption feature based on the level of the spectrum in bands on either side, and measures the strength of the feature relative to the pseudo-continuum (Worthey et al. 1994; Worthey & Ottaviani 1997). The combined metallicity index,  $[MgFe]'$ , was then determined from these values, having been selected due to its negligible dependence on the  $\alpha$ -element abundance (González 1993; Thomas, Maraston & Bender 2003). The  $H\beta$  feature was also corrected for contamination from emission by using the  $[OIII]_{\lambda 5007}$  emission line strength in the relation

$$\Delta(H\beta) = 0.6 \times EW[OIII]_{\lambda 5007} \quad (3)$$

(Trager et al. 2000), where the  $[OIII]_{\lambda 5007}$  index was measured from the residual spectrum obtained by subtracting the best combinations of stellar templates produced by PPF from the original bulge and disc spectra. For this sample, the majority of the corrections were only of the order of  $\sim 5$  per cent of the  $H\beta$  index. The

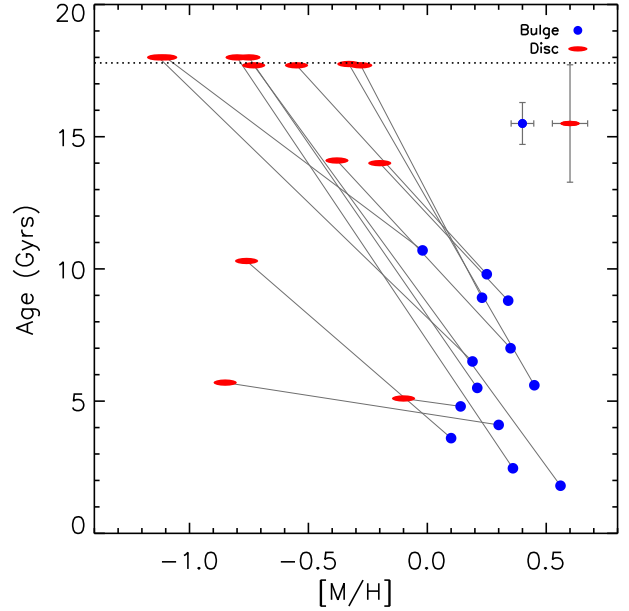


**Figure 4.** Estimates of the relative ages and metallicities of the bulges (blue circles) and discs (red ellipses) of the Virgo Cluster S0s. The solid lines link bulge and disc stellar populations from the same galaxy, and the horizontal dotted line links the lower edge of the SSP models used. The mean errors on the bulge and disc measurements are shown on the right of the plot.

uncertainties in the line index measurements were estimated from the propagation of random errors and the effect of uncertainties in the line-of-sight velocities.

Single Stellar Population (SSP) models are often used to convert line index values into quantitative measures of age and metallicity. The SSP models adopted in this study are those of Vazdekis et al. (2010), which uses the MILES stellar library. The library spectra have a resolution of  $\sim 58.4 \text{ km s}^{-1}$ , and are convolved with a Gaussian of the appropriate dispersion to reproduce the spectral resolution of the data using a web-based tool<sup>3</sup>, thus providing SSP models that are matched to the data and minimizing the loss of information that normally occurs when degrading the data to match lower-resolution models. In the case of VCC 698, the velocity dispersion of the galaxy was lower than that of the library spectra, and so the decomposed spectra of this galaxy were instead broadened to  $58.4 \text{ km s}^{-1}$ . Figure 3 shows the example of an SSP model grid for this galaxy, with the line index measurements for the bulge and disc over-plotted. The global, luminosity-weighted ages and metallicities of the bulge and disc can be calculated by interpolating across the SSP model grid. Clearly in this example the bulge appears to contain a younger and more metal-rich stellar population than the disc.

This analysis was applied to all galaxies that were decomposed with the simple bulge plus disc model outlined in Section 3, with each semi-major axis compared independently where possible as a test of the reproducibility of the results. In general it was found that the line index measurements for the bulge and disc were consistent when compared for both halves of each galaxy. Hence, single measurement for the properties of the bulge and disc stellar populations was derived for each such galaxy by taking the mean value

<sup>3</sup> <http://miles.iac.es/>

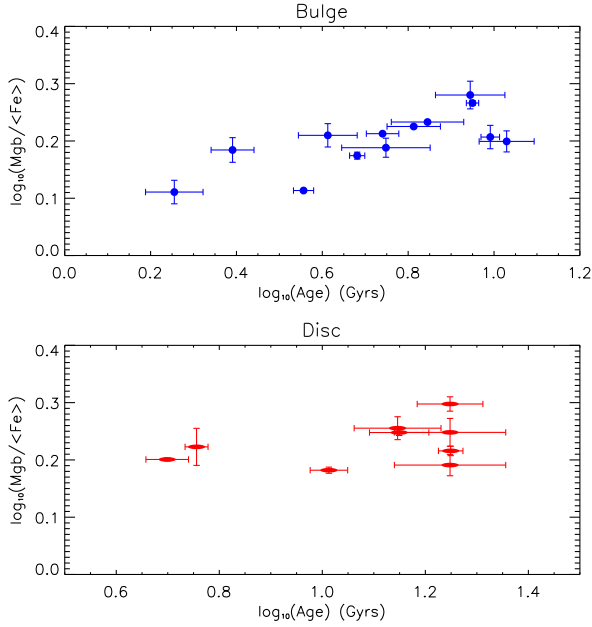


**Figure 5.** The bulge (top) and disc (bottom)  $\text{Mgb}/\langle\text{Fe}\rangle$  ratios plotted against their ages. Note that in the bottom plot, galaxies with disc ages greater than the upper limit of the SSP models have been omitted.

of the line indices from each semi-major axis. Figure 4 shows the results of this stellar population analysis for the decomposed Virgo Cluster galaxies, where the bulge results are represented by circles, the disc results by ellipses, and the lines link bulge and disc results from the same galaxy. Where the line index measurements lay off the SSP grid, the corresponding stellar populations were estimated by extrapolation, except where the  $\text{H}\beta$  line index fell below the SSP model, in which case that component was assigned a nominal age of 18 billion years. It is important to note that currently different SSP models give different absolute results due to the remaining uncertainties in stellar astrophysics, and therefore the results shown in Fig. 4 should be considered as constraints on the relative ages and metallicities of the different stellar populations rather than their absolute values. The mean errors in the bulge and disc measurements shown in Fig. 4 are derived from a combination of the difference between the stellar populations from both semi-major axes, the statistical uncertainties seen in Fig. 3, and interpolation errors when interpreting the SSP models.

Figure 4 clearly shows that the bulges contain systematically younger and more metal rich stellar populations than the discs, implying that they hosted more recent formation activity than the discs. Such recent central star formation activity after the disc was quenched would explain why S0s have been found to host positive age and negative metallicity gradients throughout their entire structure, while the precursor spirals show old bulges surrounded by a young disc.

## 4.2 Measuring $\alpha$ -enhancement

A further constraint on the stellar populations of the bulges and discs is offered by their  $\alpha$ -enhancement, as this quantity provides information about the timescales for star formation in these two components. Nucleosynthesis models predict that a significant proportion of  $\alpha$ -elements present in the ISM are ejected from Type II supernovae (SNe), whereas Type Ia SNe tend to enrich the ISM

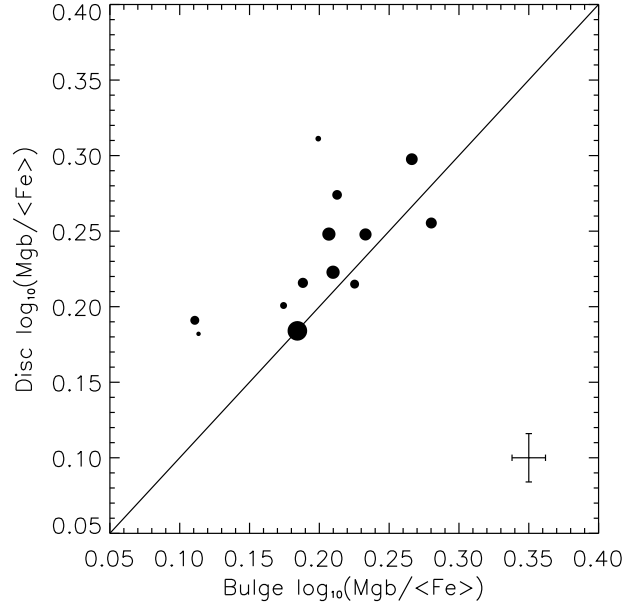


**Figure 6.** The  $\text{Mgb}/\langle\text{Fe}\rangle$  ratios for the bulge and disc of each galaxy. The size of the symbol represents the luminosity of the galaxy in the K-band, where larger symbols indicate brighter galaxies. The mean error for the data points is given in the bottom right.

with Fe (Thomas, Maraston & Bender 2003). Since Type II SNe start to occur shortly after star formation has begun while Type Ia SNe need longer for their progenitor stars to evolve, the  $\alpha$ -element abundance tells us about the star formation timescale of a stellar population.

The ratio of the Lick  $\text{Mgb}$  index over the mean of the Lick  $\text{Fe}5270$  and  $\text{Fe}5335$  indices was selected as a robust proxy of the  $\alpha$ -element abundance. Short star-formation events are characterized by larger values of this quantity,  $\text{Mgb}/\langle\text{Fe}\rangle$ , with the ratio decreasing for star formation timescales of longer than  $\sim 1$  Gyr due to the increasing Fe enrichment on such timescales.

Since this analysis directly compares measurements of the line indices for all galaxies simultaneously, all the decomposed bulge and disc spectra were broadened to match the resolution of VCC 2000, the galaxy with the highest velocity dispersion in this sample. Note that this step is not necessary when studying the stellar populations of each galaxy independently, as in Section 4.1. Figure 5 presents the  $\text{Mgb}/\langle\text{Fe}\rangle$  ratio for each decomposed spectrum plotted against the age of the bulge and disc. It can be seen that the bulge spectra show increasing  $\text{Mgb}/\langle\text{Fe}\rangle$  ratios with increasing ages; a Spearman rank test on these data shows a correlation coefficient of 0.64, implying a greater than 98 percent confidence that these quantities are correlated. This enhanced Fe enrichment in the younger bulges suggests that the enriched gas that fed the most recent star-formation events in these bulges had been contaminated by exposure to a longer period of star formation than in the older bulges. The disc spectra, on the other hand, show no obvious correlations between their  $\text{Mgb}/\langle\text{Fe}\rangle$  ratios and their ages; since many of the discs were found to be old (see Fig. 4), their light will not be dominated by the latest star-formation event, but instead represents the sum of all the stellar populations within the entire disc, so any similar correlation might be expected to be completely washed out.

Interestingly, a comparison of the bulge and disc  $\text{Mgb}/\langle\text{Fe}\rangle$  ratios, shown in Fig. 6, does reveal a correlation, with a correlation



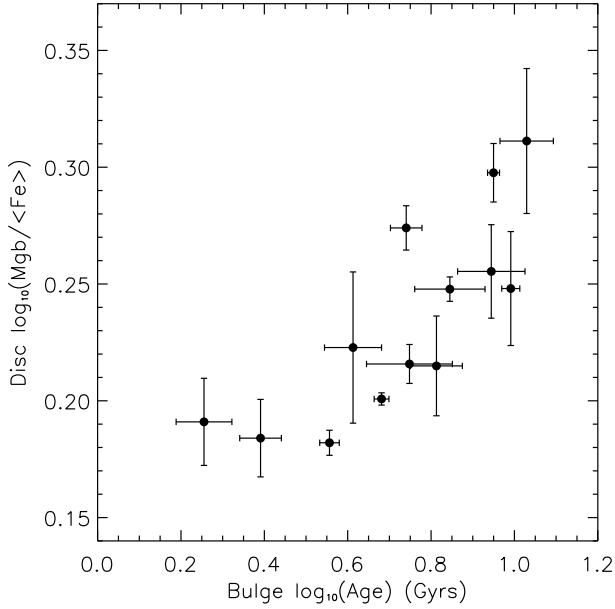


**Figure 7.** The relationship between the disc  $\text{Mgb}/\langle\text{Fe}\rangle$  relative abundances and the age of the corresponding bulges, which acts as an indicator of when the final episode of star formation occurred in that galaxy.

coefficient of 0.69 and a greater than 99 percent significance. This correlation suggests that the bulge and disc star formation histories are connected, but also shows that bulges are in general more Fe enriched than the discs of the same galaxy. This result is consistent with a scenario where the gas that produced the final star-formation event in the bulge was pre-enriched by earlier star formation within the disc. Further evidence for this scenario appears in Fig. 7, which clearly links the age of the bulges to the  $\text{Mgb}/\langle\text{Fe}\rangle$  ratios of their surrounding discs, such that galaxies with older bulges had the star formation in their discs truncated longer ago and after a shorter timescale.

## 5 DISCUSSION

In this paper, by decomposing Virgo Cluster S0 galaxies into clean disc and bulge spectra, we have been able to uncover a number of new facts about these individual components as well as the connections between them. From these data, a coherent quantitative picture of each S0’s star-formation history is beginning to emerge, which we summarize in cartoon form in Fig. 8. The galaxy starts out as a normal spiral, with an old bulge surrounded by young, star-forming disc. At some traumatic point in the galaxy’s life, the gas in the disc is stripped, thus quenching the star formation there, and in the process some of the gas gets dumped in the centre of the galaxy leading to a final burst of star formation in the bulge. The galaxy then fades to the S0 that we see today with a predominantly younger and more metal rich bulge surrounded by an older and more metal poor disc, as so clearly found in Fig. 4. Although strong indications of this phenomenon have been found previously through radial variations in age and metallicity in S0 galaxies, this study confirms that the phenomenon can be traced to the superposition of distinct bulge and disc components rather than more general gradients within those components.

A subtler probe of the star formation histories of bulges and

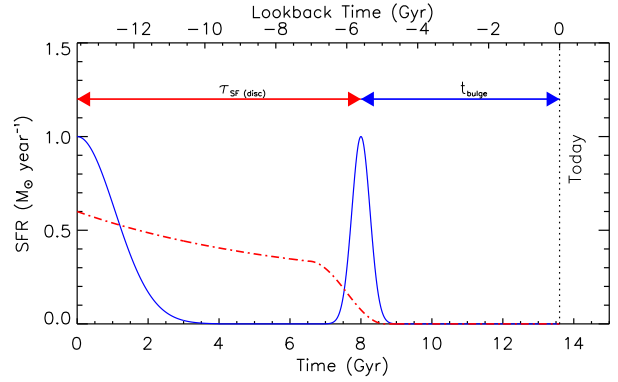


**Figure 8.** A simplified star formation history for the bulge and disc of an S0 galaxy, showing the relationship between the age of the bulge stellar populations,  $t_{\text{bulge}}$ , and the star formation timescale of the disc,  $\tau_{\text{SF}(\text{disc})}$ . The disc (dot-dash line) experiences continuous star formation, the rate of which declines gradually with time, until the quenching process begins, which finishes soon after when a central star-formation event uses up the remaining disc gas to produce the predominantly-young bulge of the final S0 (solid line).

discs is provided by their  $\alpha$ -element abundances. As we saw in Fig. 5, there is a significant correlation between  $\text{Mgb}/\langle\text{Fe}\rangle$  and age in the bulges of these galaxies, but not in their discs, which can both be understood in the context of Fig. 8. The emission from the bulge is dominated by the younger stars from the final burst of star formation, so the value of  $\text{Mgb}/\langle\text{Fe}\rangle$  is largely dictated by the gas from which this burst formed, which in this picture originated in the disc and was dumped into the bulge when the galaxy transformed. Thus, it reflects the properties of the gas in the disc at the end of its star-forming life. In general, the longer ago this transformation occurred (and hence the older the age inferred for the bulge), the shorter the star-forming lifetime of the disc because  $\tau_{\text{SF}(\text{disc})} + t_{\text{bulge}}$  in Fig. 8 reflect the total age of the galaxy. If  $\tau_{\text{SF}(\text{disc})}$  is relatively short (so  $t_{\text{bulge}}$  is relatively long), the gas left at the end of the disc’s star-forming lifetime will not be so polluted by Fe from type Ia SNe, so  $\text{Mgb}/\langle\text{Fe}\rangle$  will be relatively large, explaining the correlation seen. In the disc, on the other hand, the observed value of  $\text{Mgb}/\langle\text{Fe}\rangle$  reflects the more extended and potentially complicated complete star-formation history of this component, as its light will not be dominated by a single star-formation event, and the derived luminosity-weighted age will be similarly complex, so the absence of any correlation in this component is not a surprise.

This connection between the polluted gas from the disc and the visible last burst of star formation in the bulge is underlined by Fig. 6, which shows the general trend that the  $\text{Mgb}/\langle\text{Fe}\rangle$  in the two components are correlated, but that the disc is less Fe-enriched than the bulge. This difference arises because the disc’s value for  $\text{Mgb}/\langle\text{Fe}\rangle$  reflects its entire star-formation history, some of which will have occurred at early times before the Type Ia SNe started producing large quantities of Fe, whereas the bulge population is dominated by stars produced from the most polluted disc gas, which will be significantly more Fe enriched. There is also an interesting hint in this figure that the most massive galaxies seem to show the least difference between  $\text{Mgb}/\langle\text{Fe}\rangle$  for discs and bulges, which would suggest an earlier transformation leading to less difference in the degree of Fe enrichment, as perhaps a new example of the “downsizing” phenomenon.

As a final illustration of the physics that underlies Fig. 8, Fig. 7 shows the clear correlation between  $M_{\text{gb}}/\langle \text{Fe} \rangle$  for the disc component and the age of the bulge. Again, this fits with the finite time available for galaxy evolution, such that if the transformation occurs later then the disc will have had time to become strongly polluted by Fe, reducing  $M_{\text{gb}}/\langle \text{Fe} \rangle$ , and the bulge will have undergone its final burst of star formation relatively recently, decreasing its luminosity-weighted measured age.

As this discussion indicates, there is now a wealth of information that can be gleaned by decomposing spectra of S0 galaxies into their bulge and disc contributions, in studying the detailed stellar population properties of these individual components. We are at the point of being able not only to put together the general picture of the quenching of disc star formation accompanied by a final episode of bulge star formation shown in Fig. 8, but also looking at the variations from galaxy to galaxy to tie down the different histories that different galaxies have witnessed. Clearly, such decompositions would be more robust if carried out in two dimensions using integral field unit (IFU) data rather than long-slit spectroscopy, and the up-coming very large IFU Mapping Nearby Galaxies at APO (MaNGA) survey in SDSS-IV promises the size of sample that will answer the remaining questions about the relative importance of different transformation mechanisms.

#### ACKNOWLEDGEMENTS

We would like to thank Martin Bureau and Sugata Kaviraj for useful discussions that helped us understand these results better, and Steven Bamford for his help with the SDSS comparisons. We would also like to thank the anonymous referee for their useful comments that helped improve this paper. This work was based on observations obtained at the Gemini Observatory, which is operated by the Association of Universities for Research in Astronomy, Inc., under a cooperative agreement with the NSF on behalf of the Gemini partnership: the National Science Foundation (United States), the Science and Technology Facilities Council (United Kingdom), the National Research Council (Canada), CONICYT (Chile), the Australian Research Council (Australia), Ministério da Ciência, Tecnologia e Inovação (Brazil) and Ministerio de Ciencia, Tecnología e Innovación Productiva (Argentina). The programme IDs were GN-2008-Q-105, GN-2009A-Q-102, GN-2010A-Q-60 and GS-2010A-Q-23.

This research made use of Montage, funded by the National Aeronautics and Space Administration's Earth Science Technology Office, Computation Technologies Project, under Cooperative Agreement Number NCC5-626 between NASA and the California Institute of Technology. Montage is maintained by the NASA/IPAC Infrared Science Archive

Funding for the SDSS and SDSS-II has been provided by the Alfred P. Sloan Foundation, the Participating Institutions, the National Science Foundation, the U.S. Department of Energy, the National Aeronautics and Space Administration, the Japanese Monbukagakusho, the Max Planck Society, and the Higher Education Funding Council for England. The SDSS Web Site is <http://www.sdss.org/>.

The SDSS is managed by the Astrophysical Research Consortium for the Participating Institutions. The Participating Institutions are the American Museum of Natural History, Astrophysical Institute Potsdam, University of Basel, University of Cambridge, Case Western Reserve University, University of Chicago, Drexel University, Fermilab, the Institute for Advanced Study, the Japan

Participation Group, Johns Hopkins University, the Joint Institute for Nuclear Astrophysics, the Kavli Institute for Particle Astrophysics and Cosmology, the Korean Scientist Group, the Chinese Academy of Sciences (LAMOST), Los Alamos National Laboratory, the Max-Planck-Institute for Astronomy (MPIA), the Max-Planck-Institute for Astrophysics (MPA), New Mexico State University, Ohio State University, University of Pittsburgh, University of Portsmouth, Princeton University, the United States Naval Observatory, and the University of Washington.

EJ acknowledges support from the STFC and the RAS.

#### REFERENCES

- Abazajian K. N. et al., 2009, *ApJS*, 182, 543  
 Barway S., Kembhavi A., Wadadekar Y., Ravikumar C. D., Mayya Y. D., 2007, *ApJ*, 661, L37  
 Barway S., Wadadekar Y., Kembhavi A., Mayya Y. D., 2009, *MNRAS*, 394, 1991  
 Beckman J., Peletier R., Knapen J., Corradi R., Gentet L., 1996, *ApJ*, 467, 175  
 Bedregal A. G., Cardiel N., Aragón-Salamanca A., Merrifield M. R., 2011, *MNRAS*, 415, 2063  
 Bekki K., Shioya Y., Couch W. J., 2002, *ApJ*, 577, 651  
 Bell E. F., de Jong R. S., 2000, *MNRAS*, 312, 497  
 Binggeli B., Sandage A., Tammann G. A., 1985, *AJ*, 90, 1681  
 Bothun G. D., Gregg M. D., 1990, *ApJ*, 350, 73  
 Cappellari M., Emsellem E., 2004, *PASP*, 116, 138  
 Cardiel N., 2010, index: Line-strength Indices in Fully Calibrated FITS Spectra. Astrophysics Source Code Library  
 Côté P. et al., 2004, *ApJS*, 153, 223  
 de Jong R. S., 1996, *A&A*, 313, 377  
 Desai V. et al., 2007, *ApJ*, 660, 1151  
 Dressler A., 1980, *ApJ*, 236, 351  
 Dressler A., Oemler A. J., Smail I., Barger A., Butcher H., Poggianti B. M., Sharples R. M., 1997, *ApJ*, 490, 577  
 Fasano G., Poggianti B. M., Couch W. J., Bettoni D., Kjærgaard P., Moles M., 2000, *ApJ*, 542, 673  
 Ferrarese L. et al., 2006, *ApJS*, 164, 334  
 Fisher D., Franx M., Illingworth G., 1996, *ApJ*, 459, 110  
 Freeman K. C., 1970, *ApJ*, 160, 811  
 González J. J., 1993, PhD thesis, Univ. California, Santa Cruz  
 Gunn J. E., Gott J. R., 1972, *ApJ*, 176, 1  
 Hook I. M., Jørgensen I., Allington-Smith J. R., Davies R. L., Metcalfe N., Murowinski R. G., Crampton D., 2004, *PASP*, 116, 425  
 Hudson M. J., Stevenson J. B., Smith R. J., Wegner G. A., Lucey J. R., Simard L., 2010, *MNRAS*, 409, 405  
 Johnston E. J., Aragón-Salamanca A., Merrifield M. R., Bedregal A. G., 2012, *MNRAS*, 422, 2590  
 Johnston E. J., Merrifield M. R., Aragón-Salamanca A., Cappellari M., 2013, *MNRAS*, 428, 1296  
 Kuntschner H. et al., 2006, *MNRAS*, 369, 497  
 Larson R. B., Tinsley B. M., Caldwell C. N., 1980, *ApJ*, 237, 692  
 Mihos J. C., Hernquist L., 1994, *ApJ*, 425, L13  
 Möllenhoff C., 2004, *A&A*, 415, 63  
 Moore B., Katz N., Lake G., Dressler A., Oemler A., 1996, *Nature*, 379, 613  
 Moore B., Lake G., Katz N., 1998, *ApJ*, 495, 139  
 Moore B., Lake G., Quinn T., Stadel J., 1999, *MNRAS*, 304, 465  
 Peletier R. F., Balcells M., 1996, *AJ*, 111, 2238  
 Peng C. Y., Ho L. C., Impey C. D., Rix H.-W., 2002, *AJ*, 124, 266  
 Peng C. Y., Ho L. C., Impey C. D., Rix H.-W., 2010, *AJ*, 139, 2097  
 Poggianti B. M. et al., 2001, *ApJ*, 563, 118  
 Pompei E., Natali G., 1997, *A&AS*, 124, 129  
 Pracy M. B. et al., 2013, *MNRAS*, 432, 3131  
 Prochaska Chamberlain L., Courteau S., McDonald M., Rose J., 2011, *MNRAS*, 412, 423

- Rodríguez Del Pino B., Bamford S. P., Aragón-Salamanca A., Milvang-Jensen B., Merrifield M. R., Balcells M., 2014, *MNRAS*, 438, 1038
- Sánchez-Blázquez P. et al., 2006, *MNRAS*, 371, 703
- Sérsic J. L., 1968, *Atlas de Galaxias Australes*. Cordoba: Observatorio Astronomico
- Sil'Chenko O. K., 2006, *Astronomical and Astrophysical Transactions*, 25, 199
- Stoughton C. et al., 2002, *AJ*, 123, 485
- Terndrup D. M., Davies R. L., Frogel J. A., DePoy D. L., Wells L. A., 1994, *ApJ*, 432, 518
- Thomas D., Maraston C., Bender R., 2003, *MNRAS*, 339, 897
- Trager S. C., Faber S. M., Worthey G., González J. J., 2000, *AJ*, 119, 1645
- Vazdekis A., Sánchez-Blázquez P., Falcón-Barroso J., Cenarro A. J., Beasley M. A., Cardiel N., Gorgas J., Peletier R. F., 2010, *MNRAS*, 404, 1639
- Worthey G., Faber S. M., González J. J., Burstein D., 1994, *ApJS*, 94, 687
- Worthey G., Ottaviani D. L., 1997, *ApJS*, 111, 377